Nano Research
2022, 15(5): 4457–4465

ISSN 1998-0124 CN 11-5974/O4
https://doi.org/10.1007/s12274-022-4115-y

Research Article

Interface synergistic effects induced multi-mode luminescence

Ronghua Ma[1,§], Chunfeng Wang[1,§], Wei Yan[1,§], Mingzi Sun[2,§], Jianxiong Zhao[3], Yuantian Zheng[1], Xu Li[1], Longbiao Huang[1], Bing Chen[3], Feng Wang[3], Bolong Huang[2] (✉), and Dengfeng Peng[1] (✉)

[1] *Laboratory of Optoelectronic Devices and Systems of Ministry of Education and Guangdong Province, College of Physics and Optoelectronic Engineering, Shenzhen University, Shenzhen 518060, China*
[2] *Department of Applied Biology and Chemical Technology, The Hong Kong Polytechnic University, Hung Hom, Kowloon, Hong Kong SAR 999077, China*
[3] *Department of Materials Science and Engineering, City University of Hong Kong, 83 Tat Chee Avenue, Hong Kong, Hong Kong SAR 999077, China*
[§] *Ronghua Ma, Chunfeng Wang, Wei Yan, and Mingzi Sun contributed equally to this work.*

Received: 7 December 2021 / **Revised:** 22 December 2021 / **Accepted:** 22 December 2021

ABSTRACT

Mechanoluminescence (ML) has become the most promising material for broad applications in display and sensing devices, in which ZnS is the most commonly studied one due to its stable and highly repetitive ML performances. In this work, we have successfully prepared the biphase ZnS on a large scale through the facile in-air molten salt protection strategy. The obtained biphase has the best ML properties, which is mainly attributed to the synergistic effects of piezo-photonic, defect, and interface dislocations. DFT calculations have confirmed that the defects activate the local S and Zn sites and reduce the energy barrier for electron transfer. The much stronger X-ray induced luminescence than the commercial scintillator is also reached. The application of ZnS particles in both papers and inks delivers superior performance. Meanwhile, ZnS particles based screen printing ink is able to directly print on paper, plastic and other carriers to form clear marks. These proposed paper and ink hold great potentials in applications of information security and anti-counterfeiting based on the multi-mode luminescence properties. This work provides a new avenue to understand and realize the high-performance multi-mode luminescence, inspiring more future works to extend on other ML materials and boosting their practical applications.

KEYWORDS

interface synergetic effects, multi-mode luminescence, mechanoluminescence, biphase engineering, anti-counterfeiting

1 Introduction

Owing to the excellent capability of converting mechanical actions into photon emissions, the development of mechanoluminescent (ML) materials has achieved significant progress in recent decades. Abundant types of ML materials have been reported, including inorganic, organic, homogenous, and heterogeneous structures, showing versatile luminescent performances, flexible modulations, and remarkable stabilities. Such superior properties endow ML materials with great potential in a wide range of state-of-the-art applications, such as information security [1–5], electronic skin [6–8], and advanced display and stress sensor technologies [9–18]. ZnS has been applied in light-emitting [19, 20], catalysis and energy conversion devices [21, 22], as well as mechano-electro-optical physics [23]. Among all the ML materials, ZnS is undoubtedly one of the most potential ML doping matrices since superior performances can be obtained by doping, which further allows many novel applications. ZnS-based phosphors with excellent photoluminescence and electroluminescence properties have already been commercialized for lighting and display devices [24–28]. In general, ZnS has two stable crystal phases of sphalerite and wurtzite at room temperature, where sphalerite is the cubic phase with centrosymmetric structure and wurtzite ZnS is the hexagonal phase with a non-centrosymmetric structure. Crystal phases engineering has been widely used for controlling mechanical and optical properties [29, 30]. Currently, the ML phenomenon was mainly observed in non-centrosymmetric wurtzite ZnS and the piezoelectric effect is believed to play a key role in the ML mechanism. When combining sphalerite and wurtzite ZnS together, the change of interfacial atomic arrangments may show great potential to induce interesting modulations of the optoelectric properties of this material.

Recently, part of ZnS-based ML materials used for the demonstration of ML properties or applications is the commercial electroluminescent ZnS phosphors [9, 31–35], in which the structure and doping concentration are designed according to the electroluminescent properties. However, the optimization of the crystal structure and doping concentrations are still unclear based on the current works. On the other hand, the synthesis process of ZnS or ZnS-based ML materials is relatively complicated, which usually requires a vacuum or special gas. Moreover, defects-doped sulfides are conventionally synthesized via the high-temperature solid-state reaction, which also needs the inert atmosphere during the synthesis of such oxidation-prone materials, resulting in high energy demands and high production costs. The molten salt method in the air is considered to be a promising synthesis strategy since it is able to prevent the easy oxidation of materials at high temperatures. At the same time, it can rapidly synthesize

Address correspondence to Bolong Huang, bhuang@polyu.edu.hk; Dengfeng Peng, pengdengfeng@szu.edu.cn

industrial-grade powders with high quality and large scale, supporting future practical applications. Recently, it has been widely used in the synthesis of a variety of new functional materials such as the two-dimensional carbides and nitrides of transition metals and the luminescent quantum dots [36–38]. However, to our knowledge, there are few reports on the applications of the molten salt method in the air for the synthesis of ML materials.

Meanwhile, the conventional anti-counterfeiting techniques usually consider the mono-mode down-shifting (DS) luminescence, which is far from satisfactory performance to guarantee the safety of data and information [39]. To address such a challenge, the multi-mode luminescence becomes more attractive due to the higher anti-counterfeiting level such as the combination of upconversion and DS luminescence. However, the utilization of mechanoluminescence with other luminescence is still limited, which shows great potential for practical applications [40]. The flexible excitation method will significantly improve anti-counterfeiting technologies. Therefore, the realization of multi-mode luminescence is still urgently demanding for broad applications.

Therefore, in this work, ZnS:Mn^{2+} biphase semiconductors have been successfully prepared via an in-air modified molten salt method. Different reaction conditions have been carefully tested to regulate and control the phase and morphology of as-prepared ZnS:Mn^{2+}. Compared with ZnS with pure sphalerite or wurtzite phase, the co-existence of both phases in Mn^{2+}-doped single ZnS particle exhibit 3–6 times stronger ML intensity with brand new luminescence features due to the formation of biphase junctions. Accordingly, PL and ML properties are tuned dramatically. The optimal ML reaction conditions have been determined to realize the mass production of ML materials. DFT calculations have unraveled the remarkable ML performances that originate from the highly defective interface, where the defects are able to activate the electron transfer and exchange capability of the host materials. Moreover, such high-performance ML phosphor has also been successfully demonstrated in the applications of anti-counterfeiting applications as ML paper or printing ink, supporting the commercialization potential. Therefore, this work has supplied a novel and advanced synthesis strategy for ZnS:Mn biphase material to realize the high ML performances and promising practical production concurrently for broad commercial applications.

2 Results and discussions

Herein, we adopt a molten salt shielded sintering process to prepare ZnS:Mn^{2+} in air, as schematically shown in Figs. 1(a) and 1(b). Compared with conventional melt salt synthesis, the reaction mixture of reactants, dopants, and salt is covered by an additional salt layer (Fig. 1(a)). As the density of ZnS (4.102 g/cm^3) is much higher than NaCl (2.165 g/cm^3), the molten salt is thus capable of preventing ZnS from oxidation by O_2 in air at high temperature since ZnS particles will sink to the bottom of the crucible (Fig. 1(b)). Thermal analysis of ZnS and NaCl raw materials were conducted in air atmosphere with the same heating speed as used in the ZnS ML phosphors synthesis of our experiments (Fig. 1(c)). The mass loss and exothermic peak at 680 °C indicate the oxidation temperature of ZnS, which is well below the melting point of NaCl (endothermic peak, 804 °C). Herein, the additional salt layer is intentionally introduced to provide protection for the reactant mixture on the surface during the heating process. Thus, ZnS will be fully shielded from the environment atmosphere, which allows the synthesis of ZnS: Mn^{2+} without the usage of high-cost inert gases. This modified melt-salt reaction system could be easily scaled for mass production. As shown in Figs. 1(d)–1(f), ZnS:3%Mn was produced at 1,010 °C for 2 h using a batch of 70 g ZnS as starting material, which is 14 times to the experiment mass amount. The reaction mechanism is quite simple with the furnace chamber and crucible volume being the main limiting factors for mass production. Notably, the molten salt system simultaneously acts as the dispersion medium for $MnCl_2$, the reaction medium for the growth of ZnS crystals, and the diffusion medium of Mn^{2+} dopants into ZnS crystals, which can effectively reduce the reaction temperature and shorten the reaction time. The energy consumption could thus be reduced dramatically compared with the conventional solid reaction. Doping of Mn^{2+} into ZnS lattice is proved by the X-ray photoelectron spectra (Fig. S1 in the Electronic Supplementary Material (ESM)).

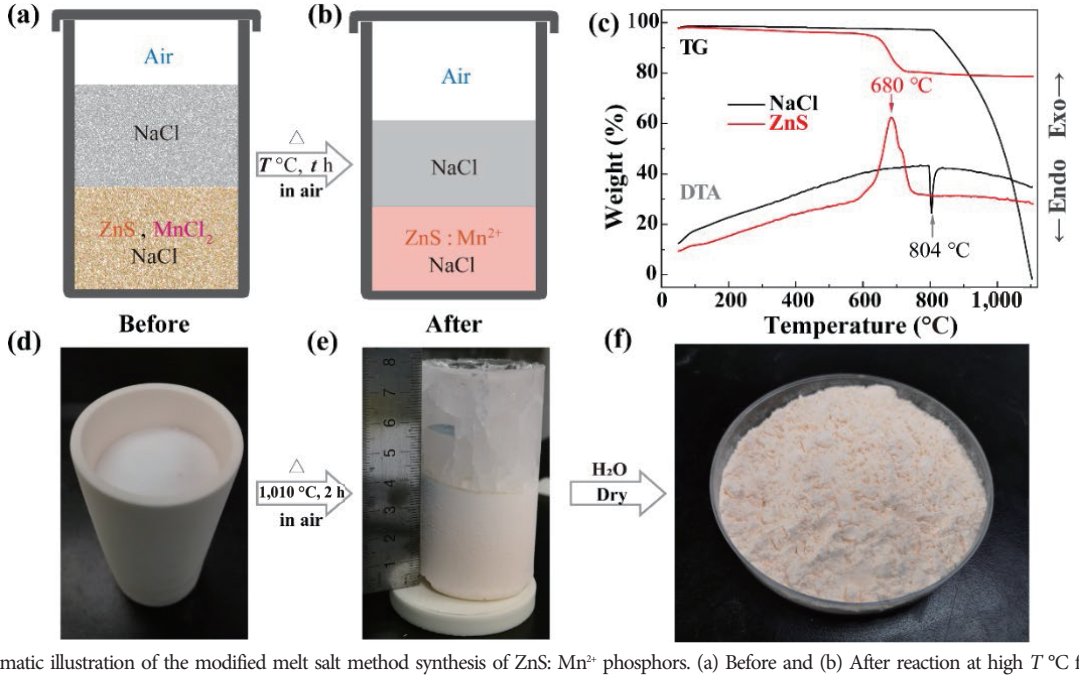

Figure 1 Schematic illustration of the modified melt salt method synthesis of ZnS: Mn^{2+} phosphors. (a) Before and (b) After reaction at high T °C for t hours. (c) Thermal analysis of NaCl and ZnS raw materials measured with a heating speed of 10 °C /min. Photos of a trial of mass production. (d) Corundum crucible filled with reaction mixture and salt. (e) Salt cylinder containing ZnS:3%Mn^{2+} product taken out from the crucible. (f) Final ZnS:Mn^{2+} phosphor.

ZnS:2%Mn were prepared at varying reaction temperatures (sample series I) or times (sample series III), the XRD patterns of sample series I are shown in Fig. 2(a), and Fig. S2 in the ESM. Pure sphalerite ZnS with a cubic structure (PDF#77-2100) is obtained at relatively low reaction temperature (800–1,000 °C) while pure wurtzite ZnS with hexagonal structure (PDF#75-1547) is obtained at a temperature higher than 1,030 °C. Synthesizing at an intermediate temperature, the coexistence of both phases is confirmed and apparently, the proportion of the wurtzite phase becomes larger with increasing temperature. Reacting at the phase-transition temperature of ZnS (1,020 °C), the continuous phase transition from sphalerite to wurtzite ZnS is observed in sample series III with a prolonging reaction time (Fig. S3 in the ESM). Correspondingly, the particle shape of both ZnS:2%Mn series shows similar transformation, as shown in the SEM images of Figs. S4 and S5 in the ESM. The micron flakes are formed in the first place, and then the granular new phase bulges gradually at the flake center till the whole flake transforms into micron particle. A typical phase transition usually contains two stages, i.e., nucleation and crystal growth. Kept at 1,020 °C for 2 h, the obtained ZnS:2%Mn is obviously in the middle of sphalerite-to-wurtzite phase-transition. While with flake shape but bi-phase nature, the ZnS:2%Mn obtained at 1,010 °C should still be in the surface nucleation stage. Overall, as depicted in Fig. 2(b), the ZnS:2%Mn particle morphology experiences dramatic changes in a narrow reaction temperature range around 1,020 °C, which happens to contain 4 typical morphologies, namely, I. Pure cubic phase at 1, 000 °C, II. Bi-phase with surface nucleation at 1,010 °C, III. Bi-phase with preferential growth in the center at 1,020 °C and IV. Pure hexagonal phase at 1,030 °C. ZnS:2%Mn were prepared at varying reaction temperatures (sample series I) or times (sample series III), the XRD patterns of sample series I are shown in Fig. 2(a), and Fig. S2 in the ESM. Pure sphalerite ZnS with a cubic structure (PDF#77-2100) is obtained at relatively low reaction temperature (800–1,000 °C) while pure wurtzite ZnS with hexagonal structure (PDF#75-1547) is obtained at a temperature higher than 1,030 °C.

Synthesizing at an intermediate temperature, the coexistence of both phases is confirmed and apparently, the proportion of the wurtzite phase becomes larger with increasing temperature. Reacting at phase-transition temperature of ZnS (1,020 °C), a continuous phase transition from sphalerite to wurtzite ZnS is observed in sample series III with prolonging reaction time (Fig. S3 in the ESM). Correspondingly, the particle shape of both ZnS:2%Mn series shows similar transformation, as shown in the SEM images of Figs. S4 and S5 in the ESM. The micron flakes are formed in the first place, and then the granular new phase bulges gradually at the flake center till the whole flake transforms into micron particles. A typical phase transition usually contains two stages, i.e., nucleation and crystal growth. Kept at 1,020 °C for 2 h, the obtained ZnS:2%Mn is obviously in the middle of sphalerite-to-wurtzite phase-transition. While with flake shape but bi-phase nature, the ZnS:2%Mn obtained at 1,010 °C should still be in the surface nucleation stage. Overall, as depicted in Fig. 2(b), the ZnS:2%Mn particle morphology experiences dramatic changes in a narrow reaction temperature range around 1,020 °C, which happens to contain 4 typical morphologies, namely, I. Pure cubic phase at 1,000 °C, II. Bi-phase with surface nucleation at 1,010 °C, III. Bi-phase with preferential growth in the center at 1,020 °C and IV. Pure hexagonal phase at 1,030 °C. Transmission electron microscopy (TEM) was conducted to further study the microstructure of ZnS particles. Two TEM samples were prepared by focused ions beam (FIB), their SEM images are shown in Fig. S6 in the ESM, sampling from the bulged center and the edge surface of one typical ZnS:2%Mn (1,020 °C, 2 h) particle, respectively (Fig. 2(c)). As shown in Fig. S7 in the ESM, the high-resolution TEM image of the bulged center clearly shows the lattice of the wurtzite ZnS phase which is validated by the fast Fourier transform (FFT) of the selected region. The particle edge was examined by TEM as well (Figs. 2(d) and 2(e)). Interestingly, the microstructure of the bi-phase junction is formed by the junction of two different crystalline ZnS phases: their lattices are validated as wurtzite ZnS in the outer layer and sphalerite ZnS inside, respectively. Noticed that abundant defects distribute at the bi-phase interface, this special structure should significantly influence the properties of such materials.

The luminescence properties of ZnS:2%Mn were investigated firstly. Under 350 nm excitation, bright broad band yellow emission centered at 590 nm is observed, which is ascribed to Mn^{2+}: $^4T_1 \rightarrow {}^6A_1$ transition, and a defect-related blue band emission

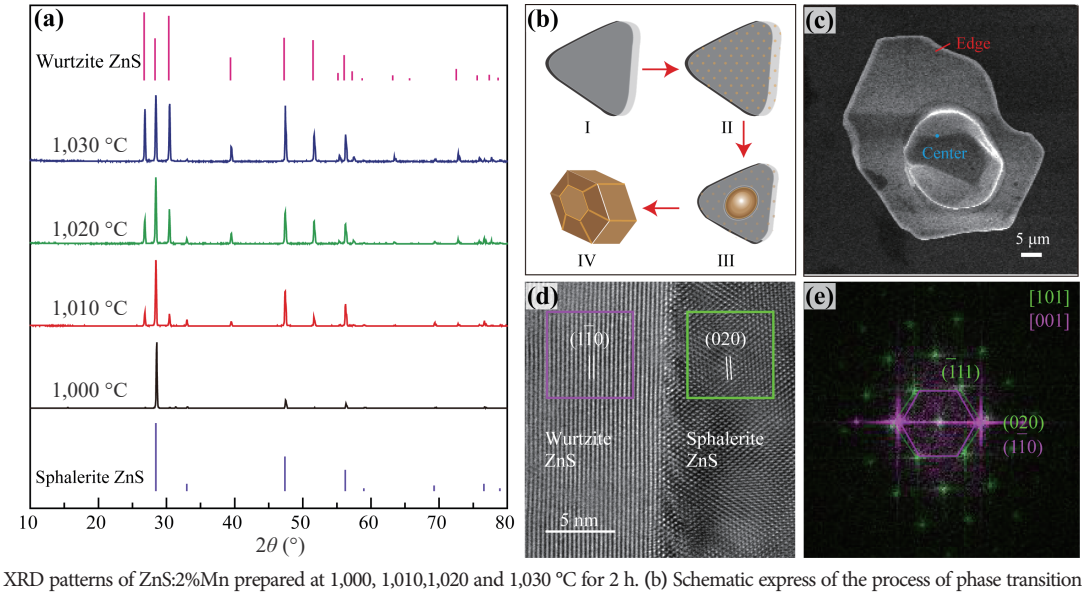

Figure 2 (a) XRD patterns of ZnS:2%Mn prepared at 1,000, 1,010,1,020 and 1,030 °C for 2 h. (b) Schematic express of the process of phase transition from sphalerite ZnS (I. S-phase) to wurtzite ZnS (IV. W-phase) through two Bi-phase ZnS states (II, III). (c) SEM image of a typical ZnS bi-phase junction structure marked with dot for center and line for edge position for further TEM observation. (d) High-resolution TEM image of a bi-phase junction cut from the edge of ZnS particle (1,020 °C, 2 h). (e) Joint diffractogram obtained by overlapping the FFT patterns of the sphalerite ZnS and wurtzite ZnS domains (indicated by the green and magenta boxes, respectively) in the crystal shown in (d).

also is observed for all ZnS:2%Mn samples prepared at varied temperatures (Fig. 3(a), and Fig. S8 in the ESM). The Mn^{2+} emission intensity increases with elevating reaction temperature due to the improved crystallinity of ZnS doping hosts. The defect emission, however, reaches its maximum during phase transition since abundant defects were generated at the bi-phase interface. Monitoring 590 nm, the excitation band around 350 nm is considered to be induced by the transition from Mn^{2+}:3d orbital to the conduction band (CB) of ZnS. Thus, compared with sphalerite ZnS:Mn, wurtzite ZnS:Mn obtained at higher temperature shows excitation band at a shorter wavelength for its wider band gap (Fig. S8(a) in the ESM), while a gradual blue-shift is witnessed near phase-transition temperature due to the formation of ZnS bi-phase junction. For a better understanding of the structure of such bi-phase ZnS junction, we first investigated the decay behaviors of pure phase ZnS:2%Mn samples by time-resolved emission spectra under 488 nm excitation. The PL intensity of pure sphalerite ZnS:2%Mn (900 °C, 2 h) decays faster at the beginning and slower subsequently compared to that of pure wurtzite ZnS:2%Mn (1,050 °C, 2 h) decaying steadily (Fig. 3(b)). Then the phosphorescence lifetime imaging (PLIM) and the phosphorescence intensity imaging (PIIM) were performed under the same excitation as well (Fig. 3(c) and Fig. S9 in the ESM). As shown in the PLIM image (inset of Fig. 3(c)), two positions are labelled, namely, spot 1 in the surrounding area with a phosphorescence lifetime of 4.61 ms and spot 2 at the center with a phosphorescence lifetime of 1.30 ms. The extracted decay curves confirm similarities between different areas of ZnS bi-phase junction and the corresponding pure phases since the same crystal structure shows similar decay behaviors.

Then we focus on ML properties of ZnS:Mn synthesized via salt-shielded melt salt method. As shown in Fig. 4(a), bright yellow light emission with a broad band centered at 590 nm owing to Mn^{2+}: $^4T_1 \rightarrow {}^6A_1$ transition was recorded when sliding on the ML film made by ZnS:3%Mn (1,010 °C, 2 h) phosphor. The integral ML intensity of ZnS:3%Mn shows a good linear relationship with the applied test forces (inset), which is a promising candidate for stress sensing applications. Further investigation was conducted in order to find the most suitable synthetic process for improved ML performances. Firstly, the influence of reaction temperature was evaluated by recording ML spectra of ZnS:2%Mn samples synthesized at T °C for 2 h under the same force of 20 N (Fig. 4(b) and Fig. S10 in the ESM). All samples herein, regardless of crystal phase, show bright yellow ML. Secondly, optimization of Mn^{2+} doping concentration was done by changing the Mn/Zn molar ratio of the raw material, synthesizing at 1,010 °C for 2 h and recording ML intensity under 20 N (Fig. 4(c)). The concentration of Mn^{2+} are 0.2%, 0.5%, 1%, 2%, 3%, 4%, 5%, 6%, 8%, 12%, and 20%. With increasing nominal doping concentration, the ML of this sample series exhibits obvious concentration effect including spectral red-shift and concentration quenching. The optimal nominal doping concentration is settled as 3 mol.%. In our previous work, the ML process in ZnS:Mn was proved to be comparable with the interband-excited PL process, especially under a weak excitation. Herein, PL spectra were tested under 300 nm excitation with both strong and weak power as well (Fig. S11 in the ESM), from which we could draw a general conclusion that PL performance is improved by elevating reaction temperature but damaged by defects formed during phase transition. Thus, one might infer that the ML enhancement in ZnS:2%Mn (1,010 °C, 2 h) is attributed to its bi-phase junction structure. This inference is verified by ML study of ZnS:2%Mn (1,020 °C, t h) series. ZnS:2%Mn (1,020 °C, 1 h), with microstructure similar to ZnS:2%Mn (1,010 °C, 2 h), exhibits brightest ML emission (Fig. S12 in the ESM), and the luminescence decay curves of the samples with Mn dopants were studied (Figs. S13 and S14 in the ESM). The decay lifetime shortens due to concentration quenching indicating that the doping concentration of Mn^{2+} in the ZnS matrix increases with growing Mn/Zn ratio, i.e., Mn^{2+} concentration in molten NaCl. As shown in Fig. 4(d), the ML mechanism in bi-phase junction ZnS:Mn is given schematically. Therefore we will present a detailed explanation of the ML enhancement mechanism in ZnS:Mn with a bi-phase junction structure. Based on these results, it's natural to conclude that ML enhancement herein is originating from promoted efficiency of mechanical excitation. On one hand, the nucleation of wurtzite ZnS on the surface of sphalerite ZnS brings in a vast amount of crystal defects. Distributing all over the phase boundary, vacancies and dislocations migrate more easily under external force, thus generating more electron-hole pairs and subsequently leading to brighter ML. On the other hand, when subjecting to external force, the built-in potential at ZnS bi-phase junction could effectively split the electron-hole pairs and boost the ZnS: CB→Mn^{2+}: 3d

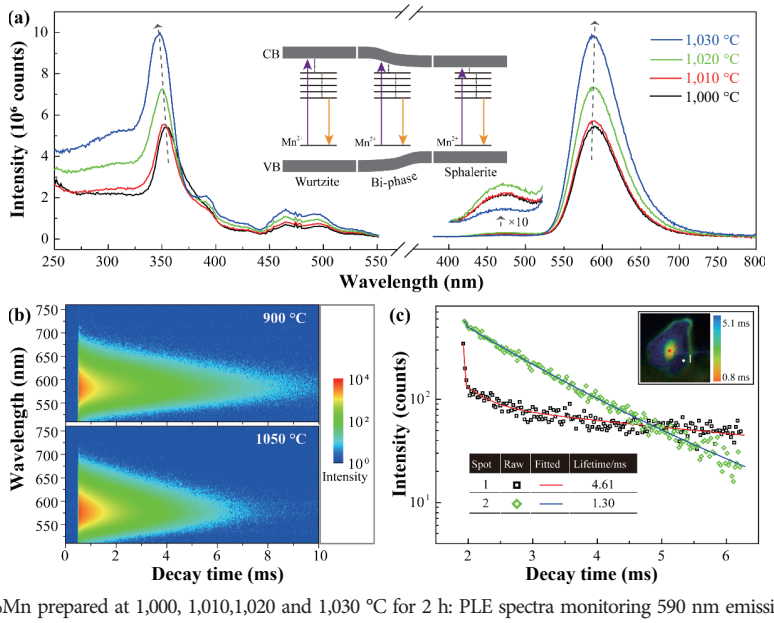

Figure 3 (a) PL study of ZnS:2%Mn prepared at 1,000, 1,010,1,020 and 1,030 °C for 2 h: PLE spectra monitoring 590 nm emission and PL spectra under 350 nm excitation. The inset gives the PL mechanism in ZnS:Mn schematically. (b) Time-resolved emission spectra of ZnS:2%Mn prepared at 900 and 1,050 °C for 2 h respectively. (c) Decay curves of two positions indicated in PLIM image of ZnS:2%Mn with a typical bi-phase junction structure (inset).

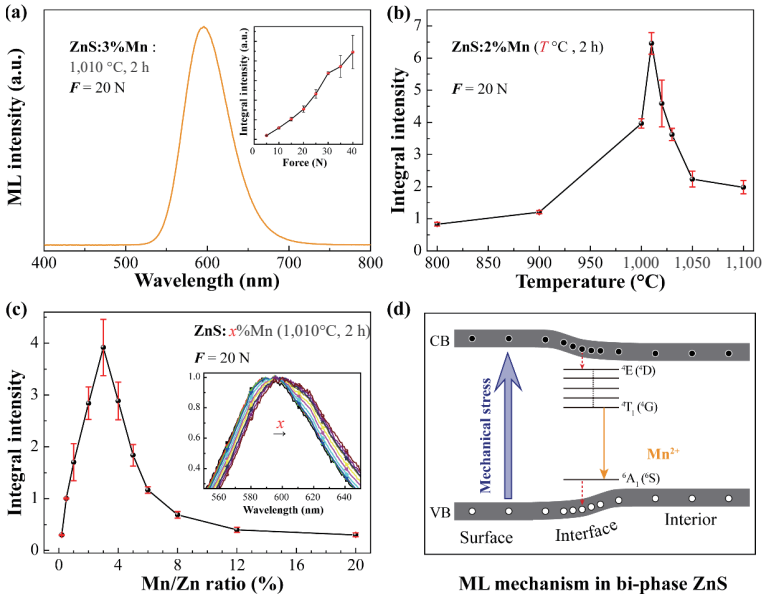

Figure 4 ML properties of ZnS:Mn. (a) ML spectra of ZnS:3%Mn prepared at 1,010 °C for 2 h and its integral ML intensity in relation to the applied test force (inset). Integral ML intensity tested by applying 20 N test force: (b) sample series I reacted at varied temperatures for 2 h; (c) sample series II with varied Mn^{2+} doping concentration, the enlarged ML spectra show red-shifting in relation to doping concentration (inset). x = 0.2, 0.5, 1, 2, 3, 4, 5, 6, 8, 12, 20. (d) ML mechanism in the bi-phase junction of ZnS:Mn.

energy transfer efficiency. Raising the reaction temperature or extending the reaction time, the consequent growth of wurtzite ZnS new phase leads to shrinking of bi-phase boundary which ends up with worsening ML performances. Based on a better understanding of ML mechanism, bi-phase junction structured ZnS:3%Mn (1,010 °C, 2 h), with optimized Mn^{2+} concentration and controlled synthesizing condition were mass-produced.

To further understand the bi-phase ZnS, we have applied DFT calculations to unravel detailed electronic structures and the promotion effect on ML performances. From the electronic distributions, the bonding orbitals near the Fermi level (E_F) are dominated by the highly defective interface between wurtzite and sphalerite phases, which play as the electroactive region to facilitate the electron transfer (Fig. 5(a)). Meanwhile, the anti-bonding orbitals locate in both wurtzite and sphalerite phases of ZnS. Such an electronic structure of the interface is induced by the abundant interface defects, which significantly promote the electron transfer for ML luminescence. Then, we have compared the detailed electronic structures of ZnS:Mn based on the projected density of states (PDOS) (Figs. 5(b) and 5(c)). For both wurtzite and sphalerite ZnS:Mn, it is noted that Zn-3d locates at the deep position near E_V–11.2 eV (E_V = 0 eV), which plays as the electron reservoir to supply sufficient electrons during the excitations by mechanical forces. S-s,p orbitals mainly contribute to valence band maximum (VBM) near E_F. On the other side, the conduction band minimum (CBM) is mainly dominated by Mn-3d orbitals, indicating an energy gap for electron transfer. Meanwhile, in the bi-phase ZnS:Mn, owing to the modulations of electronic structure, the VBM has been slightly suppressed and the Mn-3d orbitals show an evident peak near the conduction band minimum (CBM), leading to a much reduced energy barrier for electrons transfer from VB to CB than that in wurtzite ZnS:Mn. Then, we further investigate the interface through the site-dependent PDOS (Fig. 5(d)). For the S-s,p orbitals, we notice a volcano trend of the electronic structures from the interior sphalerite phase towards the surface wurtzite phase. Due to the modulation of the interface, the S-s,p orbitals have been evidently upshifted from E_V–5.40 eV in the interior sphalerite phase towards the peak at E_V–2.47 eV at the interface region. When further moving towards the surface layer, the dominant peak of s,p orbitals gradually downshifts to E_V–4.51 eV. This indicates that the S-s,p orbitals have been activated through the interface constructions with defects agglomerations. cThe Zn-3d orbitals have also been affected by the defects-dominated interface (Fig. 5(e)). Notably, the Zn-3d orbitals exhibit similar activation through the efficient p-d couplings with S sites. Compared with the individual parts of wurtzite and sphalerite ZnS, the Zn-3d orbitals have been significantly uplifted over 2.0 eV, which supports the evident promotion effect induced by the electroactive interface. These results confirm that the high concentration of defects in the interface enables evident improvements on the ML. For the Mn-3d orbitals at different parts of the bi-phase ZnS:Mn systems, we notice that limited influence has been induced by the interface (Fig. 5(f)). The stable Mn-3d orbitals have confirmed that the significant improvements of ML originate from the modulations of host materials by interface construction with a high concentration of defects. Then, we further compared the formation energies of common defects relative to the S vacancy at the interface (Fig. 5(g)). Notably, at the same chemical potential, the formation of Zn vacancies near both phases is highly favorable. Moreover, the strong formation preference of point defects further leads to the stabilization of defect complexes such as Schottky defect V_{ZnS}, unraveling the high possibility of defect agglomerations at the interface. Based on DFT calculations, we have proposed the corresponding mechanism to understand the remarkable ML performance of bi-phase ZnS:Mn (Fig. 5(h)). Due to the construction of bi-phase ZnS:Mn, sufficient defects have formed and agglomerated at the interface, which not only activates both Zn and S sites but also accelerates the electron transfer efficiency. The formation of bi-phase ZnS:Mn enables the intrinsic activation of the host materials to effectively transfer the energy from the mechanical force towards the Mn sites, which guarantees significantly improved ML performances.

In order to further explore the multi-luminescent properties of the bi-phase material, we also tested the X-ray induced luminescence of bi-phase ZnS. Under X-ray irradiation, the samples of pure cubic phase (900 °C), bi-phase (1,010 °C), and pure hexagonal phase (1,050 °C). All samples emit strong orange fluorescence, as shown in Fig. S15(a) in the ESM. While the samples of the mono-hexagonal phase emit brighter luminescence,

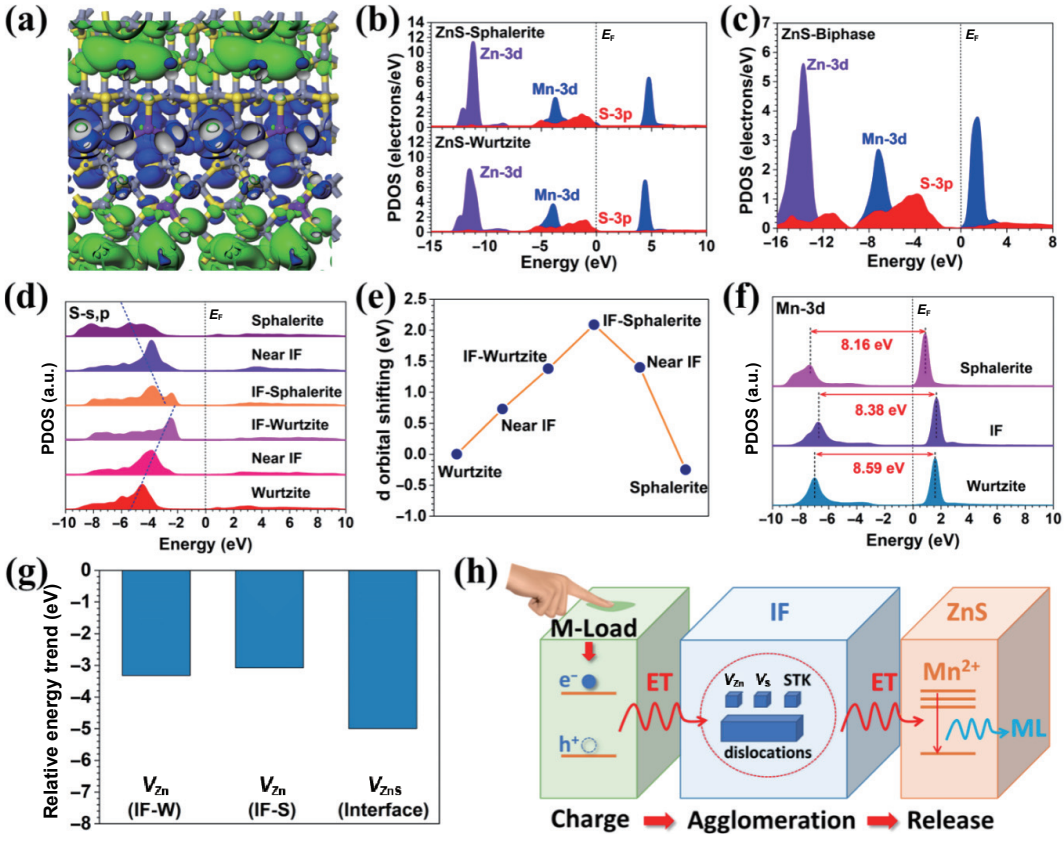

Figure 5 (a) The 3D contour plot of bonding and anti-bonding orbitals near Fermi level in Bi-phase ZnS: Mn. Grey balls = Zn, yellow balls = S and purple balls = Mn. (b) PDOS of wurtzite and sphalerite ZnS:Mn. (c) PDOS of bi-phase ZnS:Mn. (d) The site-dependent PDOS of s,p orbitals in S sites. (e) The evolution of Zn-3d orbitals in bi-phase ZnS:Mn. (f) The site-dependent PDOS of Mn-3d orbitals. (g) The relative formation energy for defects at the interface. (h) The schematic diagram for the remarkable ML performances of The site-dependent PDOS of s,p orbitals in S sites.

which is confirmed by the corresponding emission spectrum (Fig. S15(b) in the ESM). It is worth noting that the bi-phase sample has a luminescence intensity similar to that of the cubic mono-phase sample, but the Mn^{2+} luminescence peak along with defect luminescent position is consistent with that of the hexagonal phase sample. In the bi-phase ZnS:Mn, the main crystal phase is cubic ZnS, which will absorb most of the external X-ray energy and produce electron-hole pairs. Subsequently, the hot-electrons in the conduction band and the holes in the valence band are transported to the bi-phase regions respectively, where they recombine and receive energy through the dopant Mn^{2+}. Then, they can produce orange light emission with slightly higher photon energy. These results further confirmed that the formation of the bi-phase sample significantly modulates the luminescence behaviors. Meanwhile, the X-ray induced fluorescence of all samples is much better than the commercial NaI:Tl scintillator phosphor (Figs. S15(c) and S16 in the ESM), indicating that ZnS: Mn crystals synthesized by our method have the potential for X-ray detection. We further studied the luminescence under different operating conditions of the X-ray source in Figs. S15(d) and S15(e) in the ESM. With the increasing voltage and energy of the X-ray generator, the number of excited electron-hole pairs is also increased, which enhances the luminescence of the sample rapidly. When the voltage is constant, there is a good linear response between fluorescence intensity and X-ray photocurrent (Fig. S15(f) in the ESM). These experimental results are more conducive to practical application.

Furthermore, we explored some novel anti-counterfeiting applications, e.g., ML paper and ML ink, utilizing their excellent ML performances. ML paper was fabricated by adding ZnS:3%Mn (1,010 °C, 2 h) ML phosphor into a wood pulp during papermaking. A commercial laser printer was used to print on this homemade ML paper directly (Fig. 6(a)). As shown by the SEM image in Fig. 6(b), ZnS:Mn ML particles were found evenly distributed in the space among the intertwined wood fibers. The particles emit yellow light while the wood fibers are transparent under a fluorescent microscope (inset), and a brighter light response to external stress could be achieved since ML from inner particles could partially penetrate the paper. The ML paper gives intense yellow light when being scratched by nails (Fig. 6(c), Movie ESM1) or cut by scissors (Fig. 6(d) and Movie ESM2) even under natural light. As shown in Fig. 6(e), the self-adhesive label sticker made from ML paper is white in color and it turns yellow under UV lamp (Fig. 6(f)) and responds to external force sensitively (Fig. 6(g) and Movie ESM3). Such ML labels could well suit the demand for the high-security anti-counterfeit label. Owing to its micro-flake morphology, ZnS:3%Mn (1,010 °C, 2 h) yellow ML phosphor could also work well as a functional additive in printing ink. The ML is so bright that could be seen in naked eyes under a normal room LED light as seen in Movie ESM4, which is the first demonstration printed ML paper for anti-counterfeiting. In order to achieve a better demonstration effect, CaZnOS:3%Ho (1,010 °C, 2 h) with green ML synthesized using the same method was introduced to the ink as well (Fig. 6(h)). The designed pattern was divided into two colors: the yellow part and the green part, which were printed successively on commercial A4 printing paper using yellow ML ink and green ML ink, respectively, as shown in Fig. 6(i). After the printing, there leaves only a faint pattern on the A4 paper (Fig. 6(j)), originating mainly from infiltration of the paper by the ink. The ML phosphor itself is hardly visible since the printed pattern only contains an ultrathin layer of ML particles. One may expect a lighter and less visible pattern if it were printed on plastics or metals. While illuminated by a UV lamp, the printed pattern becomes clearly visible (Fig. 6(k)). Moreover, yellow or

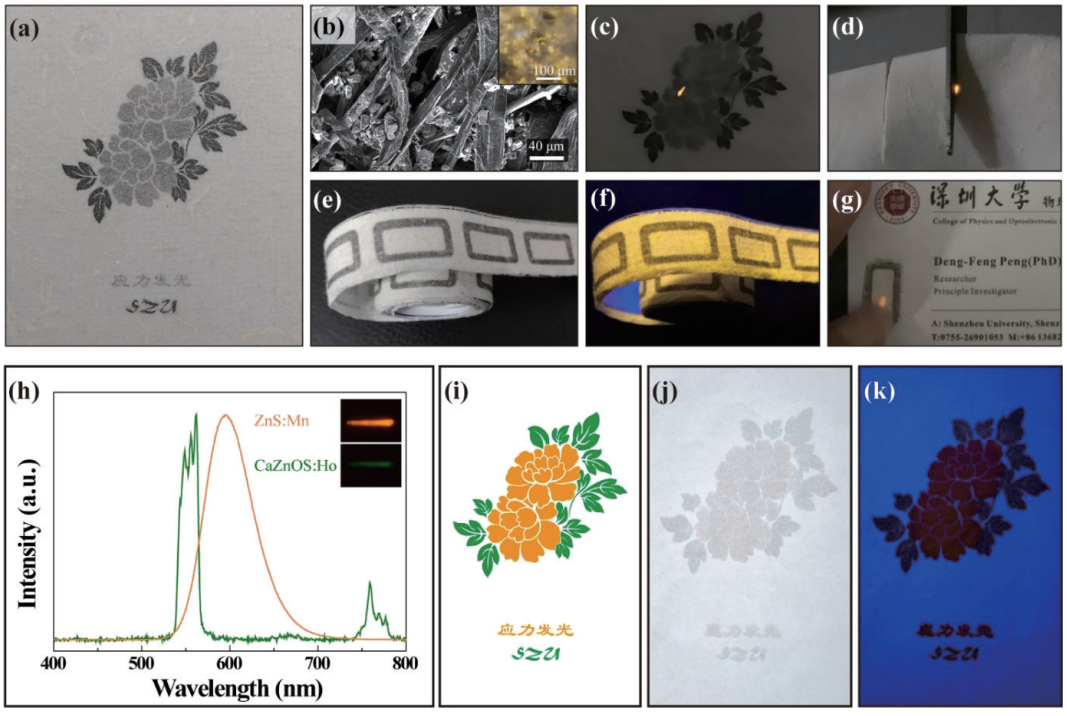

Figure 6 Application of the ML phosphor in anti-counterfeiting: (a) The photo of ML paper made in the laboratory with directly inkjet-printed patterns. (b) SEM and (inset) fluorescent microscope images of a dried paper-making mixture of ML phosphor and wood pulp. ML recorded during (c) scratching on the back of the printed pattern and (d) cutting the paper by scissors. ML label illuminated by (e) daylight and (f) 365 nm UV lamp and (g) its usage in anti-counterfeiting. Application of the ML phosphor in ML ink: (h) Normalized ML spectra of ZnS:Mn and CaZnOS:Ho prepared via the similar molten salt method, the inset shows the corresponding photos of ML under 20 N. (i) the designed screen printing pattern: 1. the flowers and Chinese characters; 2. the leaves and letters "SZU". Photos of the A4 paper after two-step screen printing patterns illuminated by (j) daylight and (k) 365 nm UV lamp.

green ML is clearly observed when scratching on the corresponding part of the pattern. In a word, such ML ink could provide high security in anti-counterfeiting printing.

3 Conclusions

Herein, we report high-performance ZnS:Mn ML phosphor and its usage in ML paper or ML ink for high-security anti-counterfeiting applications. A more economical salt shielded melt-salt method that allows synthesis in air was adopted both in experimental preparation and mass production. Sphalerite, wurtzite, and several bi-phase coexisted ZnS:Mn were prepared by controlling the synthesis conditions. While ZnS:Mn is proved mechanoluminescent regardless of crystalline phases, ZnS:Mn with special bi-phase junction morphology exhibits the best ML performance. The mechanism could be explained as follows: The mechanical excitation is enhanced by numerous crystal defects at the phase boundary, and the energy transfer (ZnS: CB→Mn^{2+}: 3d) efficiency is improved in the presence of built-in potential at the bi-phase junction. Based on the best ML phosphor, i.e., ZnS:3%Mn (1,010 °C, 2 h) ML paper and ML ink were fabricated. It is worth noting that they both show important application prospects in high-security anti-counterfeiting. DFT calculations have investigated the detailed electronic structures of the biphase ZnS, where the interface with abundant defects has activated the electroactivity of the interface through effective p-d couplings, leading to improved ML performances. Our approach to high-performance ZnS biphase semiconductor enables the adjustment of ZnS phase (homojunction) and the resulted performances. This is the first-time report for ML materials prepared via the molten salt method in air, which has a series of advantages, such as eliminating special gas, lower temperature, without grinding, etc. Most importantly, the phase of the products can be controlled and tuned, leading to the biphase homojunction semiconductor with excellent performance. This work has further extended the feasible strategy to optimize the ML performances through promising phase control techniques, which will undoubtedly benefit future research in this field.

4 Experimental Methods

Synthesis of ML phosphors via a salt-shielded melt-salt method. We choose ZnS:Mn^{2+} as the host materials because of its well-known ML properties. In addition, molten salt method has been confirmed as effective technology to shielded synthesis of oxidation prone materials in air. High purity of ZnS, NaCl and $MnCl_2{\cdot}4H_2O$ were used as starting materials. In a typical experimental procedure, 5 g ZnS, 5 g NaCl, and $MnCl_2{\cdot}4H_2O$ with designed molar ratio to ZnS are ground together in an agate mortar for 10 min. The mixture was transferred into a corundum crucible and covered by 10 g NaCl fine powder (ground for 10 min). The raw materials were heated up to T °C with a speed of 10 °C/min, and kept for t hours in a muffle furnace, and then cooled down naturally. The obtained samples were thoroughly washed in deionized water to remove the salt. Dried in an oven at 80 °C, the remained samples were used for subsequent characterizations without further treatment. The detailed design of experiments is divided in 3 series with changing reaction temperature, Mn^{2+} nominal concentration (mole ratio of Mn to Zn) and reaction time, as listed in Table S1 in the ESM.

ML film fabrication. A "suspension deposition" method is applied to fabricate the ML film for ML test and exhibition. In a typical case, 0.2g ML powder and 0.06 g UV curing adhesive (LEAFTOP 9307) were ultrasonically dispersed in ethanol, followed by a rapid transfer into a 3 cm × 3 cm square frame stainless mold placed on one piece of the EVA-covered PET film in a laminating film (Deli, No. 3817). The mold was removed after the volatilization of ethanol, then the two pieces of EVA-covered PET films were fold together very carefully. Subsequently, the film was exposed in UV light to solidify the adhesive and then

packaged by going through a thermal laminator.

ML paper fabrication. ML paper is fabricated by ML powder and plant fiber via traditional papermaking technology. Wet paper pulp was obtained through mechanical stripping, chemical dissociation and bleaching of the raw plant fibers. Paper pulp (with ~40 wt.% water) was first mixed with ML powder (5–15 wt.%) and PVA (10 wt.%) via stirring and grounding. Crosslinking of ML powder and plant fiber was formed by the long-chain PVA macromolecule. Then, 50–100 times its weight of pure water was added into the mixture. A homogeneous suspension was obtained through continuous stirring. Press the mesh screen (mesh diameter 1 mm) at about 45 degree angle into the paper slurry (The thickness of the ML paper could be controlled by the immersion depth), adjust the screen to horizontal direction, and then lift it up slowly. After draining the excess water, a hydrophobic plastic plate was used to compact the paper. Dried naturally for 24 h, the ML paper was carefully peeled from the screen.

ML ink and silk-screen printing. The specific screen-printing inks were made by dispersing 10 g of ZnS:Mn or CaZnOS:Ho ML powder with 50 mL commercial screen-printing ink which is clear and colorless liquid consisting of organic solvent and adhesives. The ink was diluted before use to obtain appropriate viscosity for printing. Via moving across the screen, a squeegee was used to transfer the ink on the screen to the object underneath through those open areas of the screen. In this work, two screens with 100 mesh sieve were used to print the designed bicolor image on commercial A4 paper. First, the flowers were printed using ink with ZnS:ML powder. After fully dried in air, the leaves were printed using ink with CaZnOS:Ho powder.

Characterization. Differential thermal analysis (DTA) and thermogravimetric (TG) analysis were simultaneously measured on a Netzsch STA409PC thermal analyzer. X-ray diffraction (XRD) patterns were recorded by a Bruker D2 phase X-ray diffraction analyzer. Photoluminescence (PL) spectra and decay were measured by Edinburgh FLS1000 spectrometer. The phosphorescence lifetime imaging (PLIM) and the phosphorescence intensity imaging (PIIM) were performed by the BH DCS-120 confocal scanning PLIM system. The ML emission spectra were recorded by a home-built measuring apparatus with a linear motor, digital Push-Pull gauge and QE65pro fiber optic spectrometer (Ocean Optics).

All intensity image and PLIM image were performed on a custom-built BH DCS-120 PLIM imaging system. In this system, a super-continuum laser with tunable pulse rate was used. Here, the wavelength λ_{ex} = 488 nm was chosen as the excitation wavelength, the detector filter was 500 nm long pass filter, the hybrid photon detector (HPM-100, Becker & Hickl GmbH., Germany) was chosen as phosphorescence detector, and a Nikon Objective (PL APO 60×/1.4 Oil) was used to imaging.

To acquire the ML spectra, we stick the ML film on a quartz glass plate firmly fixed on the table. On the front side, a digital Push-Pull gauge with a metal attachment is fixed on a platform connected to a linear motor. On the backside, the fiber connected with QE65pro fiber optic spectrometer is fixed on the same platform over against the metal attachment. The acting force of the metal attachment on ML film is tuned by the Push-Pull gauge and the movement of the platform is controlled by the programmed linear motor. During the test, the motion of metal attachment on ML film generates light emission while the fiber collects the signal synchronously.

Calculation setup. To investigate the electronic structures of bi-phase ZnS: Mn, we have utilized DFT calculations within CASTEP packages for all the calculations [41]. To achieve accurate descriptions of the exchange-correlation energy, we applied the generalized gradient approximation (GGA) and Perdew-Burke-Ernzerhof (PBE) in all the calculations [42–44]. Meanwhile, we have set the cutoff energy of the plane-wave basis to be 380 eV based on the ultrafine quality. Meanwhile, we choose the ultrasoft pseudopotentials with the Broyden-Fletcher-Goldfarb-Shannon (BFGS) algorithm. For the k-point settings, we have applied the coarse quality for the energy minimizations [45]. To accomplish the geometry optimizations, we have set the following convergence criteria: the Hellmann-Feynman forces on the atom should not exceed 0.001 eV/Å, the total energy difference should be less than 5×10^{-5} eV/atom, and the inter-ionic displacement should not exceed 0.005 Å.

Acknowledgements

The authors gratefully acknowledge the support of the National Key R&D Program of China (2021YFA1501101), National Natural Science Foundation of China (Nos. 61875136, 21771156, and 52002246), Fundamental Research Project of Guangdong Province (No. 2020A1515011315), and the Guangdong Provincial Science Fund for Distinguished Young Scholars (No.22050000560), Shenzhen Fundamental Research Project (No. JCYJ20190808170601664), Science and Technology Innovation Project of Shenzhen Excellent Talents (No. RCBS20200714114919006), and Scientific Research Foundation as Phase II construction of high level University for the Youth Scholars of Shenzhen University 2019 (No. 000002110223), the National Natural Science Foundation of China/RGC Joint Research Scheme (N_PolyU502/21) and the funding for Projects of Strategic Importance of The Hong Kong Polytechnic University (Project Code: 1-ZE2V).

Electronic Supplementary Material: Supplementary material (further details of the material characterizations, ML luminescence properties, X-ray excited luminescence properties) is available in the online version of this article at https://doi.org/10.1007/s12274-022-4115-y.

References

[1] Wang, X. D.; Zhang, H. L.; Yu, R. M.; Dong, L.; Peng, D. F.; Zhang, A. H.; Zhang, Y.; Liu, H.; Pan, C. F.; Wang, Z. L. Dynamic pressure mapping of personalized handwriting by a flexible sensor matrix based on the mechanoluminescence process. *Adv. Mater.* **2015**, *27*, 2324–2331.

[2] Zhang, J. C.; Pan, C.; Zhu, Y. F.; Zhao, L. Z.; He, H. W.; Liu, X. F.; Qiu, J. R. Achieving thermo-mechano-opto-responsive bitemporal colorful luminescence via multiplexing of dual lanthanides in piezoelectric particles and its multidimensional anticounterfeiting. *Adv. Mater.* **2018**, *30*, 1804644.

[3] Du, Y. Y.; Jiang, Y.; Sun, T. Y.; Zhao, J. X.; Huang, B. L.; Peng, D. F.; Wang, F. Mechanically excited multicolor luminescence in lanthanide ions. *Adv. Mater.* **2019**, *31*, 1807062.

[4] Ren, W.; Lin, G. G.; Clarke, C.; Zhou, J. J.; Jin, D. Y. Optical nanomaterials and enabling technologies for high-security-level anticounterfeiting. *Adv. Mater.* **2020**, *32*, 1901430.

[5] Chen, B.; Zhang, X.; Wang, F. Expanding the toolbox of inorganic mechanoluminescence materials. *Acc. Mater. Res.* **2021**, *2*, 364–373.

[6] Xu, C. N.; Watanabe, T.; Akiyama, M.; Zheng X. G. Artificial skin to sense mechanical stress by visible light emission. *Appl. Phys. Lett.* **1999**, *74*, 1236–1238.

[7] Qian, X.; Cai, Z. R.; Su, M.; Li, F. Y.; Fang, W.; Li, Y. D.; Zhou, X.; Li, Q. Y.; Feng, X. Q.; Li, W. B. et al. Printable skin-driven mechanoluminescence devices via nanodoped matrix modification. *Adv. Mater.* **2018**, *30*, 1800291.

[8] Wang, C. F.; Peng, D. F.; Pan, C. F. Mechanoluminescence materials for advanced artificial skin. *Sci. Bull.* **2020**, *65*, 1147–1149.

[9] Xiang, X. Q.; Lin, H.; Li, R. F.; Cheng, Y.; Huang, Q. M.; Xu, J.;

Wang, C. Y.; Chen, X. Y.; Wang, Y. S. Stress-induced $CsPbBr_3$ nanocrystallization on glass surface: Unexpected mechanoluminescence and applications. *Nano Res.* **2019**, *12*, 1049–1054.

[10] Wang, X. D.; Peng, D. F.; Huang, B. L.; Pan, C. F.; Wang, Z. L. Piezophotonic effect based on mechanoluminescent materials for advanced flexible optoelectronic applications. *Nano Energy* **2019**, *55*, 389–400.

[11] Wang, X. D.; Ling, R.; Zhang, Y. F.; Que, M. L.; Peng, Y. Y.; Pan, C. F. Oxygen-assisted preparation of mechanoluminescent ZnS: Mn for dynamic pressure mapping. *Nano Res.* **2018**, *11*, 1967–1976.

[12] Peng, D. F.; Wang, C. F.; Ma, R. H.; Mao, S. H.; Qu, S. C.; Ren, Z. B.; Golovynskyi, S.; Pan, C. F. Mechanoluminescent materials for athletic analytics in sports science. *Sci. Bull.* **2021**, *66*, 206–209.

[13] Luo, J. J.; Gao, W. C.; Wang, Z. L. The Triboelectric nanogenerator as an innovative technology toward intelligent sports. *Adv. Mater.* **2021**, *33*, 2004178.

[14] Zhuang, Y.; Xie, R. Mechanoluminescence rebrightening the prospects of stress sensing: A Review. *Adv. Mater.* **2021**, *33*, 2005925.

[15] Zhuang, Y.; Tu, D.; Chen, C.; Wang, L.; Zhang, H.; Xue, H.; Yuan, C.; Chen, G.; Pan, C.; Dai, L. et al. Force-induced charge carrier storage: a new route for stress recording. *Light Sci. Appl* **2020**, *9*, 182.

[16] Chen, C. J.; Zhuang, Y. X.; Tu, D.; Wang, X. D.; Pan, C. F.; Xie, R. J. Creating visible-to-near-infrared mechanoluminescence in mixed-anion compounds $SrZn_2S_2O$ and SrZnSO. *Nano Energy* **2020**, *68*, 104329.

[17] Chen, C.; Zhuang,Y.; Li, X.; Lin, F.; D. Peng, D.; Tu, D.; Xie, A., Xie, R.-J. Achieving remote stress and temperature dual-modal imaging by double-lanthanide-activated mechanoluminescent materials. *Adv. Funct. Mater.* **2021**, *31*, 2101567.

[18] Chen, W.; Zhuang, Y.; Chen, C.; Lv, Y.; Wang, M.-S.; Xie R.-J. Lanthanide-doped metal-organic frameworks with multicolor mechanoluminescence. *Sci. China Mater.* **2021**, *64*, 931.

[19] Won, Y. H.; Cho, O.; Kim, T.; Chung, D. Y.; Kim, T.; Chung, H.; Jang, H.; Lee, J.; Kim, D.; Jang, E. Highly efficient and stable InP/ZnSe/ZnS quantum dot light-emitting diode. *Nature* **2019**, *575*, 634–638.

[20] Kim, T.; Kim, K. H.; Kim, S.; Choi, S. M.; Jang, H.; Seo, H. K.; Lee, H.; Chung, D. Y.; Jang, E. Efficient and stable blue quantum dot light-emitting diode. *Nature* **2020**, *586*, 385–389.

[21] Hou, X. Y.; Peng, T.; Cheng, J. B.; Yu, Q. H.; Luo, R. J.; Lu, Y.; Liu, X. M.; Kim, J. K.; He, J.; Luo, Y. S. Ultrathin ZnS nanosheet/carbon nanotube hybrid electrode for high-performance flexible all-solid-state supercapacitor. *Nano Res.* **2017**, *10*, 2570–2583.

[22] Liu, Y. C.; Gu, Y. S.; Yan, X. Q.; Kang, Z.; Lu, S. N.; Sun, Y. H.; Zhang, Y. Design of sandwich-structured ZnO/ZnS/Au photoanode for enhanced efficiency of photoelectrochemical water splitting. *Nano Res.* **2015**, *8*, 2891–2900.

[23] Oshima, Y.; Nakamura, A.; Matsunaga, K. Extraordinary plasticity of an inorganic semiconductor in darkness. *Science* **2018**, *360*, 772–774.

[24] Guo, W. S.; Yang, W. T.; Wang, Y.; Sun, X. L.; Liu, Z. Y.; Zhang, B. B.; Chang, J.; Chen, X. Y. Color-tunable Gd-Zn-Cu-In-S/ZnS quantum dots for dual modality magnetic resonance and fluorescence imaging. *Nano Res.* **2014**, *7*, 1581–1591.

[25] Yang, C. H.; Chen, B. H.; Zhou, J. X.; Chen, Y. M.; Suo, Z. G. Electroluminescence of giant stretchability. *Adv. Mater.* **2016**, *28*, 4480–4484.

[26] Tan, Y. J.; Godaba, H.; Chen, G.; Tan, S. T. M.; Wan, G. X.; Li, G. J. X.; Lee, P. M.; Cai, Y. Q.; Li, S.; Shepherd, R. F. et al. A transparent, self-healing and high-κ dielectric for low-field-emission stretchable optoelectronics. *Nat. Mater.* **2020**, *19*, 182–188.

[27] Ji, J. P.; Perepichka, I. F.; Bai, J. W.; Hu, D.; Xu, X. R.; Liu, M.; Wang, T.; Zhao, C. B.; Meng, H.; Huang, W. Three-phase electric power driven electroluminescent devices. *Nat. Commun.* **2021**, *12*, 54.

[28] Shi, X.; Zuo, Y.; Zhai, P.; Shen, J. H.; Yang, Y. Y. W.; Gao, Z.; Liao, M.; Wu, J. X.; Wang, J. W.; Xu, X. J. et al. Large-area display textiles integrated with functional systems. *Nature* **2021**, *591*, 240–245.

[29] Yue, Y. H.; Gao, Y. F.; Hu, W. T.; Xu, B.; Wang, J.; Zhang, X. J.; Zhang, Q.; Wang, Y. B.; Ge, B. H.; Yang, Z. Y. et al. Hierarchically structured diamond composite with exceptional toughness. *Nature* **2020**, *582*, 370–374.

[30] Chen, J. W.; Wang, J.; Xu, X. B.; Li, J. H.; Song, J. Z.; Lan, S.; Liu, S. N.; Cai, B.; Han, B. N.; Precht, J. T. et al. Efficient and bright white light-emitting diodes based on single-layer heterophase halide perovskites. *Nat. Photonics* **2021**, *15*, 238–244.

[31] Peng, D. F.; Chen, B.; Wang, F. Frontispiece: Recent advances in doped mechanoluminescent phosphors. *ChemPlusChem* **2015**, *80*, 1209–1215.

[32] Wong, M. C.; Chen, L.; Tsang, M. K.; Zhang, Y.; Hao, J. H. Magnetic-induced luminescence from flexible composite laminates by coupling magnetic field to piezophotonic effect. *Adv. Mater.* **2015**, *27*, 4488–4495.

[33] Wong, M. C.; Chen, L.; Bai, G. X.; Huang, L. B.; Hao, J. H. Temporal and remote tuning of piezophotonic-effect-induced luminescence and color gamut via modulating magnetic field. *Adv. Mater.* **2017**, *29*, 1701945.

[34] Patel, D. K.; Cohen, B. E.; Etgar, L.; Magdassi, S. Fully 2D and 3D printed anisotropic mechanoluminescent objects and their application for energy harvesting in the dark. *Mater. Horiz.* **2018**, *5*, 708–714.

[35] Song, S.; Song, B.; Cho, C. H.; Lim, S. K.; Jeong, S. M. Textile-fiber-embedded multiluminescent devices: A new approach to soft display systems. *Mater. Today* **2020**, *32*, 46–58.

[36] Srivastava, V.; Kamysbayev, V.; Hong, L.; Dunietz, E.; Klie, R. F.; Talapin, D. V. Colloidal chemistry in molten salts: Synthesis of luminescent $In_{1-x}Ga_xP$ and $In_{1-x}Ga_xAs$ quantum dots. *J. Am. Chem. Soc.* **2018**, *140*, 12144–12151.

[37] Dash, A.; Vaßen, R.; Guillon, O.; Gonzalez-Julian, J. Molten salt shielded synthesis of oxidation prone materials in air. *Nat. Mater.* **2019**, *18*, 465–470.

[38] Kamysbayev, V.; Filatov, A. S.; Hu, H. C.; Rui, X.; Lagunas, F.; Wang, D.; Klie, R. F.; Talapin, D. V. Covalent surface modifications and superconductivity of two-dimensional metal carbide MXenes. *Science* **2020**, *369*, 979–983.

[39] Zhou, B.; Yan, L.; Tao, L. L.; Song, N.; Wu, M.; Wang, T.; Zhang, Q. Y. Enabling photon upconversion and precise control of donor-acceptor interaction through interfacial energy transfer. *Adv. Sci.* **2018**, *5*, 1700667.

[40] Wu, C.; Zeng, S. S.; Wang, Z. F.; Wang, F.; Zhou, H.; Zhang, J. C.; Ci, Z. P.; Sun, L. Y. Efficient mechanoluminescent elastomers for dual-responsive anticounterfeiting device and stretching/strain sensor with multimode sensibility. *Adv. Funct. Mater.* **2018**, *28*, 1803168.

[41] Clark, S. J.; Segall, M. D.; Pickard, C. J.; Hasnip, P. J.; Probert, M. I. J.; Refson, K.; Payne, M. C. First principles methods using CASTEP. *Z. Kristallogr.* **2005**, *220*, 567–570.

[42] Perdew, J. P.; Burke, K.; Ernzerhof, M. Generalized gradient approximation made simple. *Phys. Rev. Lett.* **1996**, *77*, 3865–3868.

[43] Hasnip, P. J.; Pickard, C. J. Electronic energy minimisation with ultrasoft pseudopotentials. *Comput. Phys. Commun.* **2006**, *174*, 24–29.

[44] Perdew, J. P.; Chevary, J. A.; Vosko, S. H.; Jackson, K. A.; Pederson, M. R.; Singh, D. J.; Fiolhais, C. Atoms, molecules, solids, and surfaces: Applications of the generalized gradient approximation for exchange and correlation. *Phys. Rev. B* **1992**, *46*, 6671–6687.

[45] Head, J. D.; Zerner, M. C. A Broyden-Fletcher-Goldfarb-Shanno optimization procedure for molecular geometries. *Chem. Phys. Lett.* **1985**, *122*, 264–270.